The Astrophysical Journal, 788:11 (15pp), 2014 June 10 doi:10.1088/0004-637X/788/1/11
© 2014. The American Astronomical Society. All rights reserved. Printed in the U.S.A.

BULGE GROWTH AND QUENCHING SINCE $z = 2.5$ IN CANDELS/3D-HST

Philipp Lang[1], Stijn Wuyts[1], Rachel S. Somerville[2], Natascha M. Förster Schreiber[1], Reinhard Genzel[1], Eric F. Bell[3], Gabe Brammer[4], Avishai Dekel[5], Sandra M. Faber[6], Henry C. Ferguson[7], Norman A. Grogin[7], Dale D. Kocevski[8], Anton M. Koekemoer[7], Dieter Lutz[1], Elizabeth J. McGrath[9], Ivelina Momcheva[6], Erica J. Nelson[10], Joel R. Primack[11], David J. Rosario[1], Rosalind E. Skelton[12], Linda J. Tacconi[1], Pieter G. van Dokkum[10], and Katherine E. Whitaker[13]

[1] Max-Planck-Institut für extraterrestrische Physik, Giessenbachstrasse, D-85748 Garching, Germany
[2] Department of Physics and Astronomy, Rutgers, The State University of New Jersey, 136 Frelinghuysen Road, Piscataway, NJ 08854, USA
[3] Department of Astronomy, University of Michigan, 500 Church Street, Ann Arbor, MI 48109, USA
[4] European Southern Observatory, Alonson de Córdova 3107, Casilla 19001, Vitacura, Santiago, Chile
[5] Center for Astrophysics and Planetary Science, Racah Institute of Physics, The Hebrew University, Jerusalem, 91904, Israel
[6] UCO/Lick Observatory, Department of Astronomy and Astrophysics, University of California, Santa Cruz, CA 95064, USA
[7] Space Telescope Science Institute, 3700 San Martin Drive, Baltimore, MD 21218, USA
[8] Department of Physics and Astronomy, University of Kentucky, Lexington, KY 40506, USA
[9] Department of Physics and Astronomy, Colby College, Waterville, ME 0490, USA
[10] Astronomy Department, Yale University, New Haven, CT 06511, USA
[11] Department of Physics, University of California at SantaCruz, Santa Cruz, CA 95064, USA
[12] South African Astronomical Observatory, Observatory Road, 7925 Cape Town, South Africa
[13] Astrophysics Science Division, Goddard Space Flight Center, Greenbelt, MD 20771, USA
Received 2014 February 3; accepted 2014 April 16; published 2014 May 16

ABSTRACT

Exploiting the deep high-resolution imaging of all five CANDELS fields, and accurate redshift information provided by 3D-HST, we investigate the relation between structure and stellar populations for a mass-selected sample of 6764 galaxies above 10^{10} $M_{\odot}$, spanning the redshift range $0.5 < z < 2.5$. For the first time, we fit two-dimensional models comprising a single Sérsic fit and two-component (i.e., bulge + disk) decompositions not only to the *H*-band light distributions, but also to the stellar mass maps reconstructed from resolved stellar population modeling. We confirm that the increased bulge prominence among quiescent galaxies, as reported previously based on rest-optical observations, remains in place when considering the distributions of stellar mass. Moreover, we observe an increase of the typical Sérsic index and bulge-to-total ratio (with median B/T reaching 40%–50%) among star-forming galaxies above 10^{11} $M_{\odot}$. Given that quenching for these most massive systems is likely to be imminent, our findings suggest that significant bulge growth precedes a departure from the star-forming main sequence. We demonstrate that the bulge mass (and ideally knowledge of the bulge and total mass) is a more reliable predictor of the star-forming versus quiescent state of a galaxy than the total stellar mass. The same trends are predicted by the state-of-the-art, semi-analytic model by Somerville et al. In this model, bulges and black holes grow hand in hand through merging and/or disk instabilities, and feedback from active galactic nuclei shuts off star formation. Further observations will be required to pin down star formation quenching mechanisms, but our results imply that they must be internal to the galaxies and closely associated with bulge growth.

Key words: galaxies: high-redshift – galaxies: stellar content – galaxies: structure

Online-only material: color figures

1. INTRODUCTION

The mechanism driving the shutdown of star-forming galaxies (SFGs), "quenching," remains one of the least understood puzzles in galaxy formation to date. In the low-redshift universe, galaxies show a bimodal color distribution, accompanied by a bimodality of morphologies (see Kauffmann et al. 2003; Strateva et al. 2001). Spiral galaxies have low bulge-to-disk ratios and are commonly the site of active star formation leading to blue colors. Passive galaxies are observed to be mostly spheroid-dominated. The color bimodality has also been observed at higher redshifts (e.g., Brammer et al. 2009; Whitaker et al. 2011). These observations have been interpreted as evolutionary paths, in which one or several quenching processes cause the SFG to become red and passive on a short timescale (see Bell et al. 2004; Faber et al. 2007). Studies of the shape of the mass function of passive galaxies over cosmic time, using large surveys such as Sloan Digital Sky Survey (SDSS), NMBS, zCOSMOS, UltraVISTA, and zFOURGE, showed that the probability for a galaxy being quenched increases with its mass (Peng et al. 2010; Brammer et al. 2011; Ilbert et al. 2013; Muzzin et al. 2013; Woo et al. 2013; Tomczak et al. 2014). Further evidence for quenching also comes from studies employing abundance matching techniques, where the cumulative abundance of galaxies is matched to that of halos using the results of cosmological dark matter simulations alongside observational constraints on the stellar mass function. Those infer low baryon fractions within dark matter halos, hinting at an efficient quenching mechanism associated with significant gas mass loss for both low and high mass galaxies (Moster et al. 2010; Behroozi et al. 2010).

Several quenching mechanisms have been proposed, which act to either remove the gas from the galaxy or prevent the existing/inflowing gas within the galaxy to form stars. For the high-mass regime of galaxies, powerful active galactic nucleus (AGN) feedback, which may be induced by galaxy mergers (e.g., Hopkins et al. 2006) or internal evolutionary processes triggered by (violent) gravitational disk instabilities (e.g., Bournaud et al. 2011), may drive energetic outflows expelling gas out of the galaxy and heating the halo. In addition, a so-called

"radio-mode" feedback may suppress the cooling of gas onto the galaxy over a longer timespan (Croton et al. 2006).

Moreover, morphological quenching, proposed by Martig et al. (2009) may switch off or reduce the efficiency of star formation in galaxies through the existence of a dominant bulge that stabilizes the gas disk against gravitational instabilities (see Saintonge et al. 2012 and Crocker et al. 2012 for observational hints in the local universe, and Genzel et al. 2014 for galaxies at high redshift). Another process proposed to be responsible for the shut down of galaxies is halo mass quenching (e.g., Birnboim & Dekel 2003; Kereš et al. 2005). In this scenario, dark matter haloes exceeding a critical mass of $M \sim 10^{12}\,M_{\odot}$ are able to stop the flow of incoming cold gas onto their central galaxies via virial shock heating, which leads to a decrease of star formation and/or suppresses star formation over longer timescales. However, at $z > z_{\rm crit}$ (with $1 < z_{\rm crit} < 3$), gas is predicted to penetrate to the central galaxy through cold streams, even in massive halos (e.g., Dekel et al. 2009).

The above quenching mechanisms could plausibly leave an imprint on the structure of galaxies, because they may lead to high central concentrations due to internal processes and/or major mergers. This idea triggered a plethora of studies investigating the relation between star formation activity (or absence thereof) and galaxy structure. Local galaxy surveys demonstrated that quiescence is strongly linked with structural and morphological parameters, such as the Sérsic index, stellar mass density, and the central velocity dispersion (Kauffmann et al. 2003, 2006; Schiminovich et al. 2007; Bell 2008; Fang et al. 2013; Cheung et al. 2012). This suggests that a high stellar mass surface density in the center of a galaxy is connected to its quenching.

Recently, high-resolution imaging facilities on board the *Hubble Space Telescope* (*HST*), including images from the NIR Wide-Field Camera 3 (WFC3), have allowed us to trace the relation between structure and stellar populations further back in cosmic time. Early studies on the basis of high-resolution *HST* imaging found a correlation between color and bulge fraction for large samples of galaxies at $z \sim 0.7$–1 (Bell et al. 2004; Weiner et al. 2005; Koo et al. 2005). The Cosmic Assembly Near-infrared Deep Extragalactic Legacy Survey (CANDELS; Grogin et al. 2011; Koekemoer et al. 2011) has played a particularly pivotal role, due to its unique combination of multi-wavelength high-resolution imaging, large sample size, and depth. A common theme of several of the early CANDELS studies is that a correlation between galaxy structure and stellar populations (a "Hubble sequence") has already been in place since at least $z \sim 2.5$ (Wuyts et al. 2011; Bell et al. 2012; Wang et al. 2012; Lee et al. 2013; see also Cheung et al. 2012). Additionally, Bruce et al. (2012) show that the majority of SFGs have disk-dominated light profiles, and passive galaxies have bulge-dominated profiles directly from decomposed bulge+disk light-profile fitting of $M > 10^{11}\,M_{\odot}$ galaxies at $1 < z < 3$. However, it should be noted that they also find a significant fraction (∼30%) of passive disk-dominated galaxies and star-forming, bulge-dominated systems in this high-mass regime. These results have set on a firmer footing the pioneering studies by Franx et al. (2008) and Kriek et al. (2009), that used ground-based data and significantly smaller samples, respectively. At all epochs beginning with at least $z \sim 2.5$, SFGs follow a relatively tight relation of 0.2–0.3 dex scatter between their ongoing star formation rate (SFR) and assembled stellar mass, with a zero point that increases with look-back time. This relation has been dubbed the "main sequence" (MS) of SFGs (Noeske et al. 2007; Elbaz et al. 2007; Daddi et al. 2007; Rodighiero et al. 2011). Typical SFGs that lie on the MS are best approximated by exponential disk profiles, while the quiescent galaxy (QG) population below the MS is better described with higher Sérsic indices (Wuyts et al. 2011; Bell et al. 2012). Common to all of the above studies, however, is that they were carried out on monochromatic (albeit mostly rest-optical) imaging, often exploiting only a subset of the entire CANDELS data set. If a galaxy component (e.g., disk) forms significantly more stars than another component (e.g., bulge), its relative weight in light can differ significantly from its contributions in more relevant physical units of stellar mass.

Deep panchromatic high-resolution imaging data sets enable us to go beyond measurements of light profiles, by reconstructing the distribution of stellar mass (see, e.g., Zibetti et al. 2009 for a detailed application to nearby galaxies). While pioneering work on pre-existing high-z data sets using the NICMOS camera on board *HST* was limited to small sample sizes (e.g., Elmegreen et al. 2009; Förster Schreiber et al. 2011), Wuyts et al. (2012) made use of resolved seven-band stellar-population synthesis modeling on a pixel-by-pixel basis of over 600 massive ($M > 10^{10}\,M_{\odot}$) SFGs at $0.5 < z < 2.5$ and found that galaxies are overall smoother and more centrally concentrated in mass than they appear in light. Caused by a combination of internal extinction and star formation history (SFH) variations (see also Guo et al. 2012; Lanyon-Foster et al. 2012; Szomoru et al. 2013; Wuyts et al. 2013), the presence of mass-to-light ratio variations within galaxies emphasizes the importance of making measurements on mass maps when characterizing the stellar structure of high-redshift galaxies. Guo et al. (2011) furthermore demonstrated that QGs at high redshift also feature color (and hence mass-to-light ratio) gradients.

In order to further shed light on the connection between galaxy structure and quenching, we reconstruct stellar mass maps of a large mass-selected sample ($>10^{10}\,M_{\odot}$) of galaxies at $0.5 < z < 2.5$ and subject those to a detailed structural analysis. For this purpose, we exploit the available multi-wavelength data in all five CANDELS/3D-HST fields with accurate redshifts from the 3D-HST survey (Brammer et al. 2012; van Dokkum et al. 2011). We do not restrict the structural measurements to one-component (Sérsic) fits, but rather explore two-component (bulge + disk) decompositions. The latter allows us to carry out a more direct comparison to semi-analytic models (SAMs; specifically those by Somerville et al. 2008, 2012, further developed by L. A. Porter et al. 2014, in preparation), whose prescriptions are formulated in units of disk and bulge components.

The paper is structured as follows. In Section 2, we give an overview of the observations and sample. The construction of stellar mass maps through resolved stellar population modeling, and the methodology to derive structural parameters, is described in Section 3. We present our observational results in Section 4, followed by a comparison with SAMs in Section 5. Finally, we summarize and discuss the implications of our findings in Section 6.

Throughout this paper, we quote magnitudes in the AB system, assume a Chabrier (2003) initial mass function (IMF), and adopt the cosmological parameters $(\Omega_M, \Omega_\Lambda, h) = (0.3, 0.7, 0.7)$.

2. DATA AND SAMPLE SELECTION

The core data set used for this work is the deep space-based *HST* imaging from the CANDELS multi-cycle treasury program

(Grogin et al. 2011; Koekemoer et al. 2011), complemented with redshift information from the 3D-HST grism survey (van Dokkum et al. 2011; Brammer et al. 2012).[14]

In order to determine galaxy-integrated masses and SFRs, we make use of additional multi-wavelength data in the CANDELS/3D-HST fields, including space-based photometry from *Spitzer*/IRAC, *Spitzer*/MIPS, and *Herschel*/PACS, and an array of ground-based facilities (see Skelton et al. 2014 for a detailed description of the *H*-selected multi-wavelength catalogs produced by the 3D-HST team).

The galaxy-integrated properties are derived following identical procedures as Wuyts et al. (2011). These include stellar masses, based on *U*- to - 8 μm broadband spectral energy distribution (SED) modeling using population synthesis models from Bruzual & Charlot (2003) and SFRs derived from a "ladder of SFR indicators." The latter method uses detected emission in either UV + PACS for PACS-detected galaxies (Lutz et al. 2011; Magnelli et al. 2013) or UV + MIPS 24 μm for MIPS-detected galaxies to compute the sum of the obscured and unobscured SFR. For galaxies lacking an infrared detection, the SFR is adopted from the best-fit SED model. We verified that consistent results are obtained when splitting star-forming and QGs based on the above measures of star formation activity or when adopting the rest-*UVJ* diagram (Wuyts et al. 2007; Williams et al. 2009)

2.1. HST Imaging

The *HST* CANDELS observations used for this study comprise high-resolution imaging in five distinct fields: GOODS-South, GOODS-North, COSMOS, UDS, and EGS, covering a total area of 625 arcmin^2. Typical limiting depths in H_{160} are 27.0 mag for CANDELS/wide and 27.7 mag for CANDELS/deep (the central halves of the GOODS fields), respectively. Additional data used for this work include pre-existing Advanced Camera for Surveys imaging in the GOODS, EGS, and COSMOS fields (Giavalisco et al. 2004; Davis et al. 2007; Koekemoer et al. 2007), plus WFC3 imaging in the Early Science Release (ERS; Windhorst et al. 2011). The available passbands are B_{435}, V_{606}, i_{775}, z_{850}, J_{125}, H_{160} for the GOODS fields, and V_{606}, I_{814}, J_{125}, H_{160} for the remaining fields. Additionally, Y_{098} imaging was available for ERS as part of GOODS-South and Y_{105} for the regions with CANDELS/Deep coverage.

All imaging used in our analysis was drizzled to a 0.″06 pixel scale. For details on the observations and data reduction, we refer the reader to Koekemoer et al. (2011) and Grogin et al. (2011).

2.2. Sample Definition

The main focus of this paper is on the structural shape of stellar mass distributions in a mass-selected sample of galaxies in the redshift range $0.5 < z < 2.5$. To this end, we apply a mass cut $M > 10^{10}\,M_{\odot}$ to select our galaxies, which is well above the mass completeness limit of the H_{160}-selected catalogs for all five fields. Our sample consequently spans a wide range of SFRs—from normal SFGs on the MS to QGs below—that already formed the bulk of their stars. For selection, we use the SED modeled galaxy-integrated mass estimates, but note that they nicely match the masses obtained by summing the resolved stellar mass distributions (see also Wuyts et al. 2012).

[14] The AGHAST G141 grism observations within GOODS-North from the GO-11600 program (PI: B. Weiner) are included in the analysis under "3D-HST" (Brammer et al. 2012).

In order to determine redshifts for the galaxies in our sample, we use ground-based spectroscopic redshift information whenever available. Otherwise, redshifts are fitted to the combination of 3D-HST grism data and broadband photometry.

The total sample comprises 6764 galaxies, of which 3839 and 2925 lie within the redshift range $0.5 < z < 1.5$ and $1.5 < z < 2.5$, respectively. In the following, these two redshift ranges are referred to as $z \sim 1$ and $z \sim 2$, respectively.

3. METHODOLOGY

3.1. Resolved SED Modeling

A detailed description of the resolved SED modeling can be found in Wuyts et al. (2012). Here, we review only the key steps involved and additional processing steps.

First, all images in the available wavelength bands are brought to the WFC3 H_{160} resolution (0.″18) by using the IRAF PSFMATCH algorithm. Next, a Voronoi-binning scheme from Cappellari & Copin (2003) is applied in order to ensure a minimum signal-to-noise ratio level of 10 for each bin in the corresponding *H*-band image. The binned multi-wavelength images are then fit with stellar population synthesis models from Bruzual & Charlot (2003), assuming a Chabrier (2003) IMF, a uniform solar metallicity, and a Calzetti et al. (2000) reddening law with visual extinctions in the range $0 < A_v < 4$. The adopted SFHs are exponentially declining, allowing for *e*-folding timescales down to 300 Myr. This choice is simplistic and may not be representative of the real SFHs (e.g., for SFGs, see Maraston et al. 2010). However, we are interested in the stellar mass, which, among SED-derived properties, is most robust against variations (and uncertainties) in model assumptions (e.g., Papovich et al. 2001; Shapley et al. 2005; Maraston et al. 2010).

In order to conduct further structural analysis using the (binned) output of this SED modeling technique, we constructed pixelized (instead of Voronoi binned) images of the stellar mass surface density distribution. First, we construct a M/L map that, within the galaxy's H_{160} segmentation map, has uniform values for pixels belonging to the same Voronoi bins. Pixels outside the segmentation map (i.e., containing sky noise and possibly faint wings of the galaxy extending below the signal-to-noise threshold) are assigned the average M/L of the nearest three Voronoi bins. The resulting expanded M/L map is then combined with the H_{160} image to construct a final mass map at full H_{160} resolution. This ensures a smooth transition of the galaxy's mass profile from the brighter central parts to the faintest regions.

3.2. Structural Parameters

In order to conduct a structural analysis of our galaxy sample, we employ the GALFIT (Peng et al. 2010) morphology fitting code to fit two-dimensional (2D) parametric models to the stellar mass distribution. For comparison purposes, we model the 2D H_{160} surface brightness distributions as well, following identical procedures.

As part of our set of models, we use single Sérsic models to parameterize the galaxy's shape with the effective radius (R_e) and Sérsic index n. R_e is the galactocentric distance containing half the total light/mass, and n is a measure of the cuspiness of the overall light/mass profile. We allow n to vary within the range $0.2 < n < 8$.

While the Sérsic index n is often used and indeed serves as an approximate measure of the contribution of the bulge, it is

important to note that n does not translate one to one to the bulge-to-total ratio, B/T (see Appendix A; also Andredakis et al. 1995; de Jong et al. 2004; Cibinel et al. 2013; Bruce et al. 2012; Bruce et al. 2014). For a given bulge + disk composite profile, the best-fit Sérsic index can be increased both by increasing the B/T, and by leaving the B/T constant while growing the extent of the disk relative to that of the bulge (i.e., lowering $R_{e,B}/R_{e,D}$). For this reason, and to facilitate a more direct comparison to (semi-analytic) models that are parameterized in terms of bulge and disk units, we furthermore decompose the galaxies by fitting two-component (bulge + disk) models. In addition, we also performed one-component pure disk and pure bulge fits by forcing $n = 1$ and $n = 4$, respectively.

For the bulge-to-disk decomposition, we adopt a procedure similar to that implemented in Bruce et al. (2012) for the bulge+disk decomposition of H_{160} light profiles, where we fixed the Sérsic indices to be $n = 1$ for the disk and $n = 4$ for the bulge.[15] The centers are left free, but we restrict the relative distance between the bulge and disk centers to be less than 2 pixels. All other parameters defining the two components (R_e, the axial ratio b/a, and the total magnitude/mass of both components) are allowed to vary independently.

In two-component modeling, the higher number of degrees of freedom increases the odds of the fit being trapped in a local χ^2 minimum. In order to mitigate this risk, we ran GALFIT using a grid of initial starting values. Our grid was constructed by using a range of size ratios between bulge and disk ($R_{e,B}/R_{e,D}$), ranging from 0.1 to 1, in steps of 0.1. For each initial guess of $R_{e,B}/R_{e,D}$, the corresponding initial guess on B/T was then set, such that the Sérsic index matching this initial configuration matches the one measured in the single-component fit (see Appendix A). Likewise, the initial magnitudes and absolute values of the initial size guesses for bulge and disk were set such that the total magnitude and half-light/mass radius of the composite profile matches the respective values determined from Sérsic fitting.

In cases where GALFIT yields solutions with implausibly small bulge sizes (<0.1 pixel, corresponding to $\lesssim$1/30 of the resolution, or $\lesssim$50 pc at $z \sim 2$) and flags the outcome as potentially not converged and unphysical, we excluded that run from the grid. Also, solutions yielding a disk smaller in size than the bulge (i.e., $R_{e,B}/R_{e,D} > 1$) were not included.[16]

After performing the fits for each point of the grid with initial guesses, we assigned a final B/T ratio for each object as the solution of the fit with the lowest $\chi^2_{\rm red}$. Here, the pure disk and pure bulge fits were also included. Their solutions generally show higher $\chi^2_{\rm red}$ than the two-component fits, but are occasionally preferred over those in a $\chi^2_{\rm red}$ sense (oftentimes, these are bulgeless systems with $n < 1$). The two-component decompositions are statistically preferred over the single Sérsic models (as based on both their $\chi^2_{\rm red}$ values and the Akaike information criterion, AIC[17]) for $\sim$2/3 of the total sample. Those systems for which the single Sérsic model yields a lower value of $\chi^2_{\rm red}$ and AIC typically feature shallow profiles with $n < 1$.

In both single- and two-component fitting, we use an automated scheme that pre-determines neighboring sources that need to be masked or fitted simultaneously, and passes initial guesses of fitting parameters to GALFIT. Those include estimates on size, total magnitude, and center. The initial guess on size is based on the distance from the center to the radius at which the curve of growth reaches 50% of the galaxy's total flux. The mass-weighted center of the galaxy derived within its segmentation map is adopted as initial estimate for the center. GALFIT takes into account the convolution of the model with the point-spread function (PSF). Both for fitting light and mass, we use a PSF that is a combination of stacked stars and a TinyTim (Krist 1995) model PSF. For a more detailed description of the used PSF, see van der Wel et al. (2012).

We emphasize that throughout this paper our working definition adopted for bulge and disk components is based on the above bulge+disk modeling of stellar mass or light maps, as there are currently no empirical constraints on whether or not stars assigned to a bulge/disk component are dynamically hot/cold. As the SINS survey of $z \sim 2$ galaxy kinematics demonstrated that high-redshift SFGs are dynamically (Förster Schreiber et al. 2009) and morphologically (Förster Schreiber et al. 2011) distinct from local spiral galaxies, we caution that bulge fractions as derived by our decompositions may have a somewhat different meaning than they would have in the local universe.

In addition, we estimated a typical measurement uncertainty on B/T by setting up an array of model galaxies with a range of mass, size, B/T ratio, and $R_{e,B}/R_{e,D}$, which is similar to our data. The grid of model galaxies consisted of 5, 3, 11, and 10 grid points in mass, R_e, B/T, and $R_{e,B}/R_{e,D}$, respectively. These were then inserted in multiple empty sky regions of the CANDELS UDS field to mimic the typical background noise.[18] We next ran GALFIT on all 8250 mock galaxies using our two-component fitting scheme. The measurement error on B/T of each galaxy in our sample given its mass, radius, and profile shape is then finally assigned as the scatter among the recovered B/T ratios of the corresponding model galaxy.

Typical measurement errors in B/T for star-forming and QGs are, on average, $\sim$0.05 and $\sim$0.06 at $z \sim 1$ and $\sim$0.1 and $\sim$0.13 at $z \sim 2$, respectively. The distribution of errors peaks below the median ($\lesssim$0.05), and shows a tail toward higher B/T errors. Two alternative methods to estimate the uncertainty in B/T, namely, the formal random uncertainty reported by GALFIT and re-fitting the observed galaxies after applying additional background and Poisson noise, generally lead to lower estimated uncertainties (by a factor of $\sim$2 in the case of GALFIT). In the remainder of the paper, we therefore adopt the most conservative error estimates inferred from our analysis of the inserted mock galaxies.

[15] Since the choice of a Sérsic index value for the bulge profile has long been debated in the literature (see Kormendy & Kennicutt 2004 and references therein), we repeated our two-component fits, with the only change fixing $n = 2$ for the bulge component to address the impact on the derived B/T values. We find a median difference of $B_{n=4}/T - B_{n=2}/T = 0.03^{+0.15}_{-0.11}$ for QGs and $0.01^{+0.09}_{-0.12}$ for SFGs, with the errors marking the 1σ scatter. Any systematic trends are small, and our results are therefore robust against the precise value of $n_{\rm bulge}$ adopted.

[16] We note that nuclear stellar disks in early-type galaxies do exist (e.g., Jaffe et al. 1994; van den Bosch et al. 1994; Ferrarese et al. 1994), but they are impossible to resolve at the *HST* resolution for $z \sim 2$ galaxies.

[17] In evaluating models with the AIC, the preferred model is the one that minimizes $\chi^2 + 2p + 2p(p+1)/N - p - 1)$, where p is the number of free parameters in the fit and N is the number of data points used in the fit.

[18] UDS is part of CANDELS-Wide, which was exposed for two *HST* orbits divided over F125W and F160W. Part of our data set comes from the CANDELS-Deep regions (the central halves of the GOODS fields), which received four orbits per pointing in F125W and F160W each. The inferred uncertainties from our analysis of mock galaxies can therefore be considered as conservative estimates.

4. RESULTS ON GALAXY STRUCTURE

4.1. The Evolving Mass Budget of Disks and Bulges

When exploiting the bulge–disk decompositions of the stellar mass maps derived for our sample of massive galaxies, we first evaluate the average mass budget of disks and bulges. The following is an example of picking a random star out of the sample of massive galaxies above 10^{10} $M_{\odot}$. At $1.5 < z < 2.5$, the probability that this star belongs to a bulge component is 46%. Increasing the mass limit to $\log(M) = 10.5$ or 11 yields a higher probability for the star to be associated to the bulge (49% and 54%, respectively). Perhaps somewhat surprisingly, the fraction of stars residing in a bulge component rises only slightly, to $0.5 < z < 1.5$ (47%, 50%, and 56%) for galaxies more massive than $\log(M) = 10$, 10.5, and 11, respectively.

The formal uncertainties to the above stated probabilities, including sample variance and typical measurement errors on B/T, are limited to a few percent. The total error budget is likely dominated by systematics, for example, related to the assumptions made in stellar population modeling (see Section 3.1). We note, however, that only M/L uncertainties with a differential impact on bulges and disks will affect the above numbers. Even if the M/L ratio of bulges were systematically under- or overestimated by 0.2 (0.3) dex with respect to those of disks, the change would be limited to ~7(10)%.

Since bulges, unlike stellar disks, can be considered sinks in the continuous assembly of a galaxy's stellar component, the rising mass density of stars in bulges (by a factor of ~1.8 from the higher to the lower redshift bin) seems to be compensated largely by the continuing assembly of new disks. Splitting our sample in finer redshift bins, we do find the fraction of stellar mass in bulges to increase more significantly, by a factor ~1.5 over the entire 6 Gyr timespan sampled in our study.

Overall, the bulge mass fractions are higher than what would be inferred from fits to the *H*-band surface brightness profiles, as the median mass-to-light ratio of disk components is 0.2 dex lower than the bulge components. The above numbers address the evolving mass budget of disks and bulges for a mass-limited sample, including both star-forming and QGs. In the remainder of the paper, we will break down our sample by star formation activity.

4.2. Profile Shape

In recent years, several *HST*-based studies have investigated the structural differences between star-forming and QGs at high redshift. In all of these analyses star-forming systems are found to have significantly larger rest-optical sizes than their quiescent counterparts at the same mass and redshift (e.g., Toft et al. 2009; van der Wel et al. 2014). In addition, their surface brightness profile shapes tend to be shallow ($n \sim 1$), whereas QGs feature cuspier light profiles (e.g., Wuyts et al. 2011; Bell et al. 2012; Cheung et al. 2012, although see also Bruce et al. 2012 for decomposed light profiles at high stellar masses and redshifts).

At the same time, the same multi-wavelength, high-resolution look-back surveys have also established that substantial mass-to-light ratio variations in the rest-optical can occur, not only between but also within galaxies (see, e.g., Wuyts et al. 2012; Guo et al. 2012; S. Boada et al. in preparation). Since new stars typically tend to form from gas settled in a disk configuration, M/L ratio variations are anticipated to give rise to a composite light profile in which the disk component has a relatively larger weight (per unit mass) than the bulge. It is therefore important to address to what degree the above structural distinction between the two classes of galaxies is intrinsic to their distribution of stellar mass, or, conversely, can be attributed to stellar population effects. The answer is of immediate relevance to our understanding of quenching, as the latter scenario could imply that compact quiescent systems can evolve from the star-forming MS by simple fading, without invoking an associated morphological transition. Kriek et al. (2009) investigate this scenario for a spectroscopically confirmed sample of massive $z \sim 2$ galaxies, finding that three out of six massive star-forming systems have dense cores, and thus may passively evolve into compact galaxies due to the fading of the outer star-forming regions. Szomoru et al. (2010), on the other hand, exploit the exquisite depth of the Hubble Ultra Deep Field to probe the surface brightness profile of a massive compact QG at $z = 1.91$, ruling out the existence of a faint extended envelope or disk around the observed galaxy. Another argument against fading comes from Cheung et al. (2012), who derived the stellar masses of bulges for both star-forming and QGs at $0.5 \leqslant z < 0.8$. They found that the bulges of SFGs are half as massive as those of similar-mass QGs, implying they cannot simply fade onto the red sequence without structural evolution.

Using the stellar mass maps reconstructed for our mass-selected sample of 6764 galaxies at $0.5 < z < 2.5$ with $\log(M) > 10$, we are now able to draw statistically significant conclusions on the structural distinction between high-z galaxies prior to and after quenching. In Figure 1, we compare the shape of the stellar mass distributions (i.e., corrected for spatial M/L variations) of star-forming and QGs, and study their dependence on the total galaxy stellar mass. We consider profile parameters based on single-component (i.e., Sérsic) fits as well as two-component (bulge + disk) decompositions, and show the results for two separate redshift intervals: $0.5 < z < 1.5$ and $1.5 < z < 2.5$. In both cases, we identified a galaxy as quiescent if its specific SFR (sSFR) satisfied $\mathrm{sSFR} < 1/3t_{\mathrm{Hubble}}$, where t_{Hubble} is the Hubble time at the redshift of the galaxy, and as star-forming otherwise. We tested that a definition of quiescence based on the location of a galaxy in the *UVJ* diagnostic diagram (Wuyts et al. 2007; Williams et al. 2009) yields effectively identical results.

Figure 1 immediately highlights that the distinct structural appearance of star-forming and QGs is intrinsic to its internal distribution of stellar mass, and not just driven by stellar population or obscuration effects. In fact, a comparison to the equivalent plots based on *H*-band surface brightness profiles rather than mass maps (see Appendix B) indicates that stellar population effects (when measuring at rest-optical wavelengths) only induce a modest, albeit non-negligible shift. At all masses, QGs feature cuspier stellar mass distributions (i.e., higher n) than star-forming systems. Their typical best-fit Sérsic index is also an increasing function of galaxy mass. Interestingly, among SFGs the profile shape is not independent of stellar mass. An increase in n is apparent above 10^{11} $M_{\odot}$, both at $z \sim 1$ and at $z \sim 2$. A similar trend of increasing cuspiness at the tip of the MS was noted by Wuyts et al. (2011, Figure 1; see also E. J. Nelson et al. in preparation).

Next, it is worthwhile to reflect on what is measured when fitting Sérsic profiles. Appendix A illustrates that, when considering galaxies as superpositions of bulge and disk components, a given best-fit Sérsic index does not necessarily correspond one-to-one to a unique B/T value, even though it is often interpreted as such. Given a bulge+disk system with an associated best-fit n, one can increase its n either by boosting B/T, or,

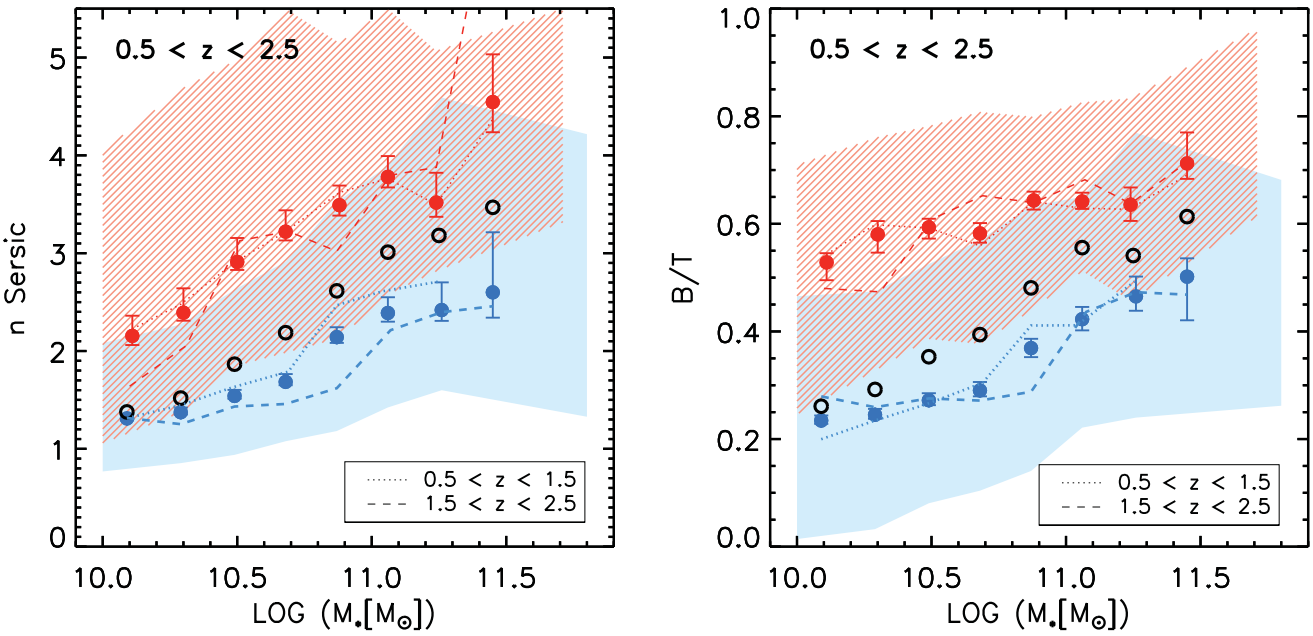

Figure 1. Sérsic index and B/T ratio as a function of the total stellar mass of our galaxy sample spanning the redshift range $0.5 < z < 2.5$. The whole sample (black non-filled symbols) is divided in star-forming (blue symbols) and quiescent galaxies (red symbols). The respective shaded areas mark the 50th percentile scatter of the distributions within one bin, while the error bars indicate the uncertainty on the median value. Results for the lower and upper halves of the redshift interval are marked with dotted and dashed lines, respectively. The bins contain (from left to right) 1439, 1091, 886, 693, 484, 259, 114, and 35 star-forming systems, and 227, 267, 298, 369, 280, 214, 83, and 25 quiescent systems within the whole redshift range. SFGs show a clear trend of increasing Sérsic index and B/T with increasing stellar mass, reaching $B/T \sim 0.4$–0.5 above $10^{11}\ M_{\odot}$ and reflecting the build-up of central mass concentrations in main-sequence SFG up to $z \sim 2.5$.

(A color version of this figure is available in the online journal.)

alternatively, by growing the extent of the disk with respect to that of the bulge without any change to B/T.

The right-hand panel of Figure 1 explores the B/T ratio as a function of galaxy mass, for SFGs and QGs separately. Again, we find a clear anti-correlation between star-formation activity and bulge prominence. Focusing on the star-forming population, the median B/T is limited to below 30% for intermediate mass SFGs ($10 < \log(M) < 11$), while typical bulge mass fractions rise to 40%–50% above $10^{11}\ M_{\odot}$. We note that there is a significant scatter in the distribution of individual B/T values around the median for both quiescent and SFGs. We investigated the variation in median trends when varying the binning intervals, finding negligible changes at lower masses, while the median B/T of the most massive ($\log(M) \sim 11.3$) SFG bin changes by ± 0.1, depending on the applied binning intervals.[19]

We note that measurements on the H band yield bulge mass fractions among SFGs that are lower by ~30% (on average), as can be understood from a disk component composed of a younger, lower M/L stellar population than the bulge.

From the two-component fits, we infer a typical $R_{e,B}/R_{e,D}$ size ratio of ~0.2, albeit with significant scatter (see Figure 6). The median size ratio shows little dependence on star-formation activity or mass, over the range probed by our sample. Given the enhanced B/T values in QGs, and the fact that bulges have smaller half-mass radii than disks, one might wonder if the difference in total size between SFGs and QGs can be completely accounted for by a redistribution of stellar material from the disk to the bulge, without changing the extent of each of the components individually. Our analysis confirms that the change in the B/T of SFGs prior to or during quenching is, to a large extent, responsible for the size difference between the quiescent and star-forming population. However, some fraction of the shrinking size is still attributed to the individual components being smaller. In Figure 2, we show the total sizes as well as the sizes of the individual components for star-forming and QGs, as measured on the mass maps. While the total sizes of SFGs and QGs are noticeably different (by a factor ~3 at $\log(M_*) \sim 10.5$), the difference in the size of the bulge and the disk components between SFGs and QGs, respectively, is smaller, typically by a factor ~1.5.

4.3. Fraction of Quenched Galaxies

With the morphological parameters of the mass maps for our entire galaxy sample in hand, we now proceed to relate those with galaxy-integrated star formation properties.

The three panels of Figure 3 show, from left to right, the fraction $f_{\rm quench}$ of quenched galaxies as a function of total stellar mass, bulge mass, and disk mass, respectively. Here, we again define galaxies as quenched/quiescent when sSFR $< 1/3 * t_{\rm Hubble}(z)$, and as star-forming otherwise.

The uncertainties in $f_{\rm quench}$ are derived via a bootstrapping method and represent the 68% confidence levels. They include sample variance and the typical measurement errors on B/T, which are derived as described in Section 3.2. For the bootstrapping, we computed $f_{\rm quench}$ for 1000 samples, which are randomly drawn from the original sample, with replacement. For each bootstrap iteration, we displace the B/T values for each galaxy by the typical measurement error in B/T, given the galaxy's magnitude, size, and measured profile shape.

The top left panel of Figure 3 illustrates that the fraction of quenched galaxies increases with increasing mass, from ~0.1 at around $10^{10}\ M_{\odot}$ to ~0.5 at $2 \times 10^{11}\ M_{\odot}$. A second conclusion

[19] The binning scheme applied in Figure 1 is such that the most massive bin still contains more than 10 galaxies, allowing a robust estimation of the median.

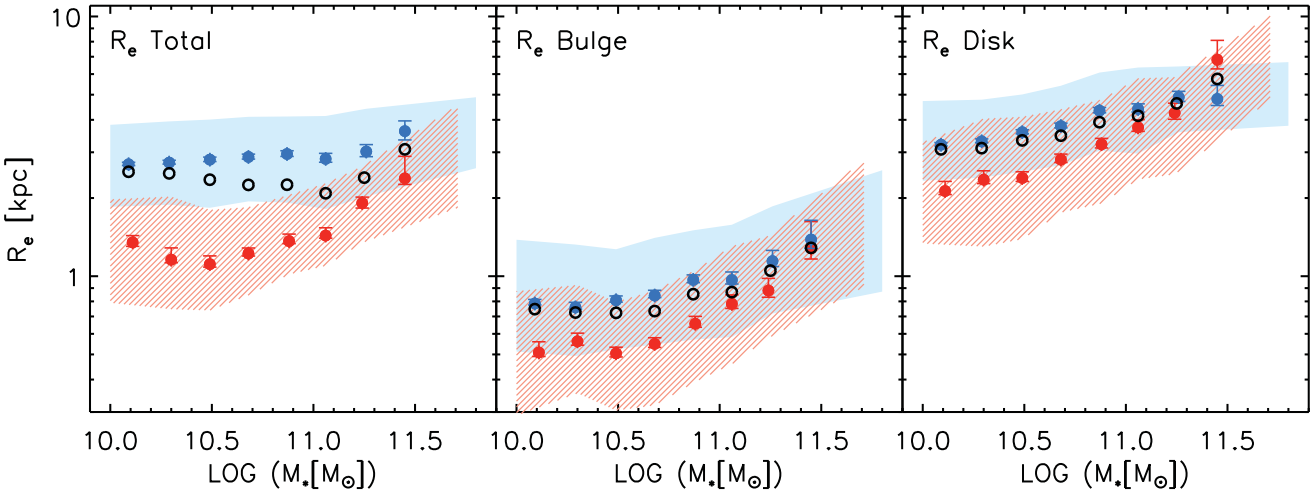

Figure 2. Effective total size, bulge size, and disk size as a function of total stellar mass in the redshift range $0.5 < z < 2.5$. The total sizes are derived from single Sérsic fits, and bulge and disk sizes are inferred from the bulge–disk decompositions. The whole sample (black symbols) is divided into star-forming (blue symbols) and quiescent galaxies (red symbols). The respective shade areas mark the 50th percentile scatter of the distributions, while the error bars indicate the uncertainty on the median value. There is a clear difference in total size between SFGs and QGs over the whole mass range. In addition, the bulge and disk components individually appear to be smaller for the star-forming population up to masses of $\log(M) \sim 11.3$.

(A color version of this figure is available in the online journal.)

is that the fraction of quenched galaxies is overall higher for the lower redshift bin, by, on average, a factor of ∼2. Both of these results are well established in the literature. The rising mass function of QGs over cosmic time has most recently been quantified on a firm statistical footing by Muzzin et al. (2013) and Ilbert et al. (2013), both of which exploit the wide-area UltraVISTA survey. What CANDELS lacks in number statistics compared to UltraVISTA, it adds in depth and high resolution. Exploiting these key strengths, we now turn to the dependence of the quenched fraction on galaxy subcomponents: the mass of their bulge (middle panel) and disk (right-hand panel). Clearly, the dependence of $f_{\rm quench}$ on the bulge mass is much stronger than on the disk mass, which does not show any significant correlation with $f_{\rm quench}$ above $\log(M_{\rm Disk}) \sim 9.5$. Toward lower disk masses, $f_{\rm quench}$ increases rapidly, but we point out that this trend is entirely driven by the (total) stellar mass limit of our sample ($\log(M_*) > 10$; that is, the galaxies occupying the lowest $M_{\rm Disk}$ bins are necessarily heavily bulge-dominated systems, which tend to form relatively few stars). If lower mass galaxies were to be included, less massive, disk-dominated SFGs would likely outnumber these massive spheroids with small residual disks in the low $M_{\rm Disk}$ bins, producing a flat relation of $f_{\rm quench}$ with $M_{\rm Disk}$ over the full range probed. Above respective masses of $10^{10}\ M_\odot$, $f_{\rm quench}$ increases more rapidly with bulge mass than with total stellar mass in both redshift ranges (∼0.35 per dex of $M_{\rm bulge}$ compared to ∼0.3 per dex M_*, or ∼0.1 per dex of $M_{\rm Disk}$).

With the bulge-to-disk decompositions in hand, we next split the galaxy sample in bins of B/T, and explore second parameter dependencies. Considering first the dependence of $f_{\rm quench}$ on the total stellar mass, it is apparent that, at a given total mass, $f_{\rm quench}$ is increasing significantly with increasing B/T ratio. The middle panels of Figure 3 illustrate that, when considering the dependence of $f_{\rm quench}$ on bulge mass, the different B/T bins align along a much tighter locus. In contrast, a large spread is seen as a function of disk mass (right-hand panels of Figure 3). In order to quantify these trends, we compute the Spearman's rank correlation coefficient (r_s) for the relations of $f_{\rm quench}$ with $\log(M_*)$, $\log(M_{\rm Disk})$, and $\log(M_{\rm bulge})$ for respective masses $\log(M) > 10$. We find that r_s is indeed significantly higher for the relation $f_{\rm quench}$ versus $\log(M_{\rm bulge})$ ($r_s \sim 0.68$), than for both $f_{\rm quench}$ versus $\log(M_*)$ ($r_s \sim 0.32$) and $f_{\rm quench}$ versus $\log(M_{\rm Disk})$ ($r_s \sim -0.05$), as measured for $z \sim 1$. Consistent results are found for $z \sim 2$.

We investigated the impact of defining quiescence based on a *UVJ* color–color criterion instead of a sSFR cut. When applying a *UVJ*-based selection of QGs, we find an overall good agreement with the trends presented in Figure 3. Quantitatively, small changes occur, with $f_{\rm quench}$ increasing by ∼7% for the entire $0.5 < z < 2.5$ sample integrated over all masses. The good agreement is not surprising, since the precise threshold in sSFR used to select QGs ($\mathrm{sSFR} < 1/3 * t_{\rm Hubble}(z)$) was chosen to yield maximum overlap with the *UVJ* selection criterion.

Taken together, this demonstrates that the build-up of a bulge seems to play a critical role in the quenching process of galaxies, whereas the disk does not. The amount of stars in the disk component of a galaxy has little to no predictive power regarding its star-forming or quenched state, unless B/T (and hence the bulge mass) is also known. We find a qualitatively similar behavior at $z \sim 2$ as at $z \sim 1$, but note that the cosmic evolution in the quiescent fraction cannot solely be attributed to continuing bulge growth over time, as galaxies in the same M_* and B/T bin at $z \sim 1$ are more likely to be quenched than those at $z \sim 2$. Appendix B illustrates how the equivalent diagrams composed from fits to the *H*-band surface brightness, rather than the stellar mass distribution, exhibit a larger spread from low to high B/T bins. This generic behavior can be understood from a physical picture, where the disk component has a relatively larger weight in light than in mass.

Our work is in agreement with, and takes the next step beyond, previous reports that the inner stellar mass density is better related to the SFH than the total stellar mass (Franx et al. 2008; Bell et al. 2012), as inferred from rest-optical imaging of smaller samples of high-redshift galaxies (see Kauffmann et al. 2003 and Fang et al. 2013 for a local universe reference, and Cheung et al. 2012 for intermediate redshifts $z < 0.8$)

Importantly, the same behavior explored here over the redshift range $0.5 < z < 2.5$ extends in a strikingly similar fashion all

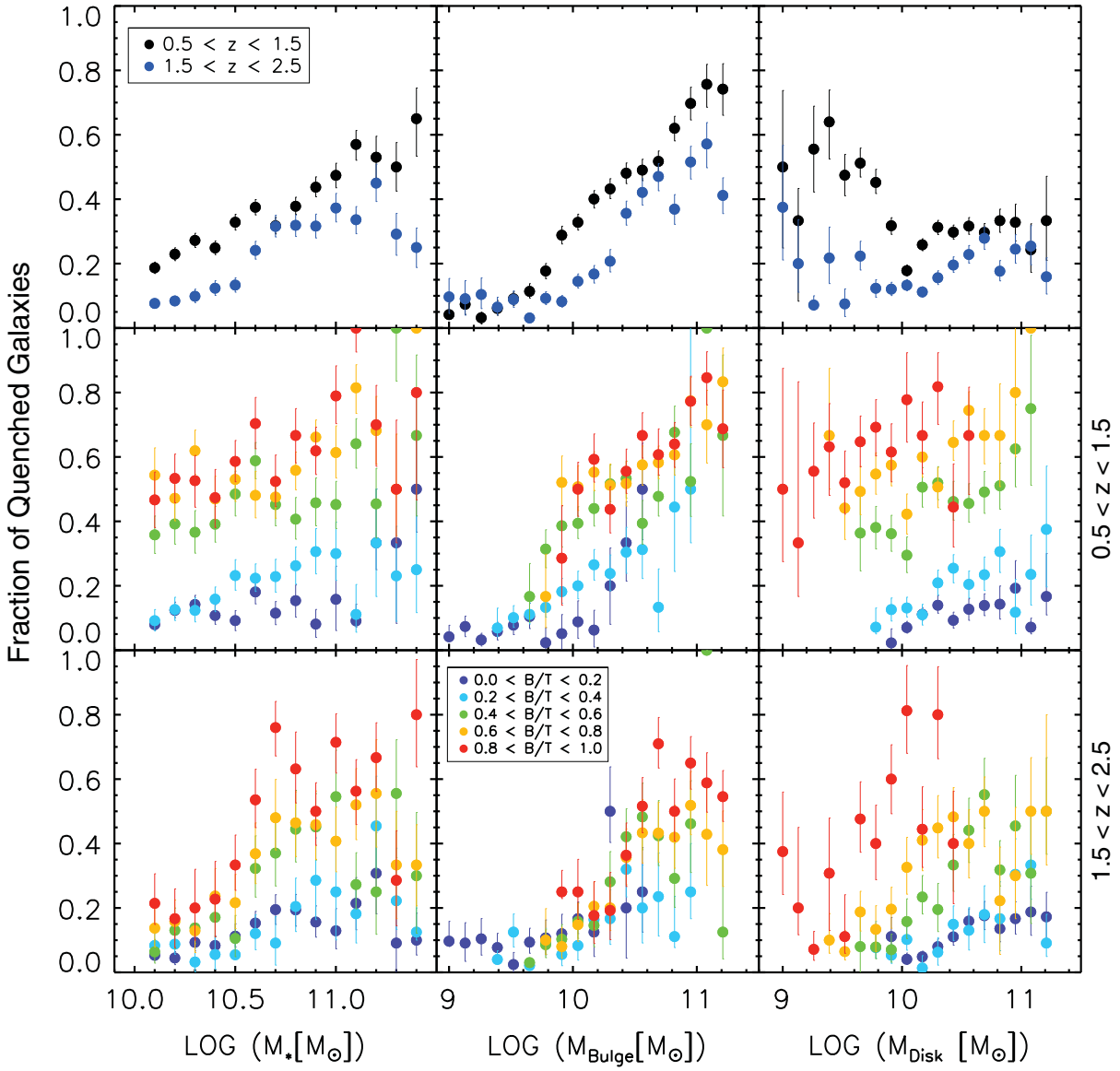

Figure 3. Fraction of massive galaxies ($M > 10^{10}\ M_{\odot}$) that are quiescent ($f_{\rm quench}$), as a function of total stellar mass (left columns), bulge mass (middle columns), and disk mass (right columns) for $z \sim 1$ and $z \sim 2$. Galaxies with sSFR $< 1/3 * t_{\rm Hubble}$ are assigned as quiescent, the others are assigned as star-forming. In the middle and bottom rows, we split the galaxy sample in bins of B/T for the two redshift bins. Uncertainties are derived from bootstrapping and include sample variance as well as measurement uncertainties. A positive trend of $f_{\rm quench}$ is seen with total stellar mass, with the trend becoming stronger when correlating $f_{\rm quench}$ with the bulge mass, whereas $f_{\rm quench}$ shows no positive correlation with the mass of the disk component. At a given galaxy mass, $f_{\rm quench}$ is increasing significantly with increasing B/T ratio. The scatter in $f_{\rm quench}$ among the different B/T bins is largely reduced when correlating against the bulge mass, implying that the mass within the bulge of the galaxy is correlating best with quiescence. This trend is qualitatively similar for both redshift ranges, with the overall quenched fractions being lower at $z \sim 2$ than at $z \sim 1$.

(A color version of this figure is available in the online journal.)

the way to the present day, as demonstrated by Bluck et al. (2014) who exploit the large number statistics of SDSS.

5. COMPARISON WITH SAMS

5.1. The Somerville Model

SAMs have a rich history of trying to reproduce galaxy scaling relations and abundances, with the goal of guiding our interpretation of the observational results. Here, we focus specifically on the SAM developed by Somerville et al. (2008) and further updated by Somerville et al. (2012) and L. A. Porter et al. (2014, in preparation), which is rooted in the Bolshoi cosmological dark matter simulation (Klypin et al. 2011).[20] As is generic to all SAMs, the model relies on simplified analytic prescriptions for the dynamical and astrophysical processes down from entire galaxy scales, rather than on kiloparsec to parsec scales (the resolution below which state-of-the-art cosmological and zoom-in hydro-simulations resort to subgrid physics, respectively). This limitation, however, yields the enhanced flexibility of a relatively inexpensive runtime, allowing the straightforward generation of statistically significant model galaxy populations, and the tuning of parameters to observational constraints, such as mass functions and scaling relations (only empirical constraints from the nearby universe were used in tuning the parameters of the model considered here). The fact that SAMs conceptually are formulated in units of bulge and disk components furthermore

[20] Hereafter, we refer to this model as the Somerville et al. SAM.

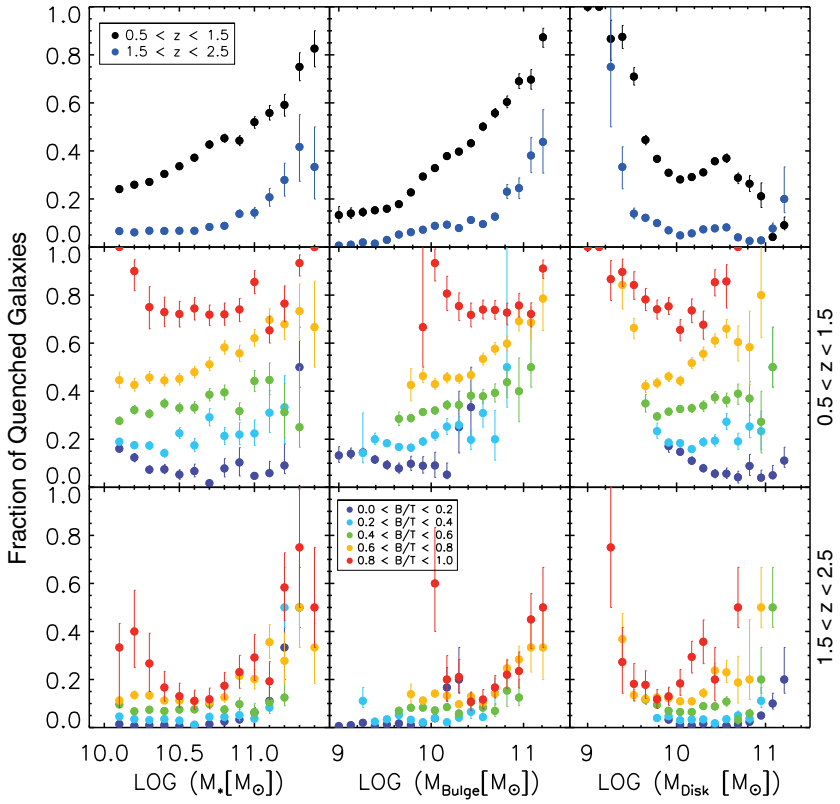

Figure 4. Same as Figure 3 using galaxies from the Somerville et al. SAM. Galaxies with sSFR $> 1/3 * t_{\rm Hubble}$ are assigned as star-forming, the others are assigned as quiescent. Uncertainties are derived via bootstrapping to reflect the sample variance.

(A color version of this figure is available in the online journal.)

makes them suitable for a direct and meaningful comparison to the diagnostics explored in this paper.

A detailed description of the prescriptions for cooling, star formation, feedback, and structural growth is provided by Somerville et al. (2008, 2012), with extensions and applications to the CANDELS data set presented by L. A. Porter et al. (2014, in preparation). The input to and output from the model is further contrasted to that of other SAMs by Lu et al. (2013).

For a detailed discussion of the physical recipes of this SAM and the resulting output in the context of a larger set of SAMs, we refer the reader to Lu et al. (2013). For the sake of the comparison presented here, we emphasize that none of the relations investigated in this paper were part of the set of observational constraints to which the model parameters were tuned. Model parameters of the SAM were tuned to (approximately) match the global stellar mass function, the stellar mass function of early- and late-type galaxies, the gas fraction as a function of stellar mass for disks, and the mass–metallicity relation for stars.

Also of particular relevance is the fact that, in the model, stars form either in the disk following a Kennicutt–Schmidt law (Kennicutt 1998), where the disk scalelength is set by a similar methodology as Mo et al. (1998), or, in the event of a merger during a starburst. Bulge formation, as well as feeding of the central supermassive black hole, can happen through two channels: mergers or disk instabilities (see L. A. Porter et al. 2014, in preparation). The starburst, black hole accretion, and morphological transformation induced by mergers depends on the mass ratio and gas fraction, as calibrated using a large suite of binary merger simulations (Somerville et al. 2008, 2012; Hopkins et al. 2009). Star formation is moderated by heating the gas by supernovae as well as through AGN feedback. In addition to the quasar mode, during which AGN can drive powerful outflows, black holes also grow more gradually over longer timespans through the so-called radio mode (i.e., suppression of cooling via radio jets). No explicit connection between the bulge mass and quenching (as may for example be expected from the Toomre Q stability criterion in a gravitational quenching scenario; see Section 6.2) was built into the model.

5.2. $f_{\rm quench}$ in the SAM

In Figure 4, we show the model equivalent of Figure 3, describing how the fraction of galaxies that are quenched depends on the total stellar mass, the mass of stars in the bulge, and the mass of stars in the disk component, respectively. As for the observations, we define the threshold for a galaxy to be quenched with a ruler moving with redshift: sSFR $< 1/(3t_{\rm Hubble})$. This definition, rather than an application of the *UVJ* diagnostic, remains closer to the direct output of the SAM, avoiding a translation to mock spectral energy distributions, which would introduce additional assumptions and uncertainties.[21]

At first glance, the SAM features several of the characteristic trends noted earlier for the CANDELS galaxies: $f_{\rm quench}$ rises toward later cosmic times, increases with the total stellar mass (more steeply so with bulge mass), and shows no appreciable

[21] It should be noted that equivalent assumptions and uncertainties associated with the conversion from light to physical properties enters upon SED modeling of the observed galaxies. The choice of how far to take the models to the observations, or vise versa, therefore remains somewhat arbitrary.

correlation with disk mass above $\log(M_{\rm Disk}) = 9.5$. In the interval $9 \lesssim \log(M_{\rm Disk}) \lesssim 9.5$, a sharp drop with increasing $M_{\rm Disk}$ is noted, as also shown in the observations. Given the $M > 10^{10}\ M_{\odot}$ threshold of our sample selection, the latter objects are necessarily heavily bulge-dominated. Without imposing such a mass limit, less massive, disk-dominated SFGs would outnumber massive early-type galaxies with small residual disks in the lower $M_{\rm Disk}$ bins. Despite the qualitative success, quantitative differences in the quenched fractions of model galaxies with respect to those observed are clearly present. The discrepancy is most severe at $z \sim 2$, where modeled $f_{\rm quench}$ values are, on average over the whole displayed mass range, of order a factor ~2–3 short of the observed, hinting at an underestimated quenching rate and/or inefficiency to prevent quiescent systems from rejuvenating.[22]

When splitting the SAM galaxies at each M_*, $M_{\rm bulge}$, and $M_{\rm Disk}$ in bins of B/T (middle and bottom panels of Figure 4), we reproduce a similar behavior as found for the real universe in Section 4.3. Namely, the total stellar mass acts as a poorer predictor of the quenched state of a galaxy. This situation can be remedied if in addition to M_*, B/T (and hence $M_{\rm bulge}$) is also known. Quantitatively, the correlation between $f_{\rm quench}$ and $M_{\rm bulge}$ is measured to be the strongest ($r_s \sim 0.46$), whereas M_* and $M_{\rm Disk}$ only show weak correlation with $f_{\rm quench}$ ($r_s \sim 0.21$ and $r_s \sim -0.1$, respectively). The quoted values of r_s are measured for respective masses of $\log(M) > 10$ and at $z \sim 1$. The values for r_s at $z \sim 2$ are similar, with the correlation between $f_{\rm quench}$ and $\log(M_*)$, as well as between $f_{\rm quench}$ and $\log(M_{\rm Disk})$, being somewhat stronger. At $0.5 < z < 1.5$, less than 20% of all massive galaxies with $B/T < 0.2$ are classified as quiescent. Conversely, the majority of galaxies in the upper B/T bin (with $B/T > 0.8$) have low sSFR. These inferences are in agreement with the SAM and the observations. Also in agreement is the fact that $M_{\rm bulge}$ serves as a better predictor of $f_{\rm quench}$ than the total stellar mass, with different B/T bins being more (albeit not perfectly) aligned along a single locus in the $f_{\rm quench}$ versus $M_{\rm bulge}$ diagram.

At $1.5 < z < 2.5$, the model predictions are skewed toward too low $f_{\rm quench}$ values, as noted earlier. However, in relative terms the same generic behavior, as a function of bulge, prominence is notable.

We note that most of the trends in Figure 4 are driven by physical prescriptions in the SAM affecting central galaxies rather than satellites, as centrals account for 80% (90%) of the model galaxy population above $\log(M) = 10$ (11). Those massive galaxies classified as satellites are further subjected to additional environmental quenching processes, resulting in a higher $f_{\rm quench}(M_*, M_{\rm bulge})$ for this particular subpopulation.

5.3. The Agent of Quenching

Given the qualitative agreement between the model and observations, we can now pose the question how, in the context of the Somerville SAM, the relation between structure and stellar populations could be interpreted. To this end, we consider the dependence of $f_{\rm quench}$ on two physical properties of galaxies in the SAM that are not observationally accessible for our CANDELS sample: the halo mass $M_{\rm Halo}$ and the mass of the central supermassive black hole $M_{\rm BH}$. The top panels of Figure 5 illustrate that the probability of a galaxy being quenched increases toward high $M_{\rm Halo}$ and high $M_{\rm BH}$. In detail,

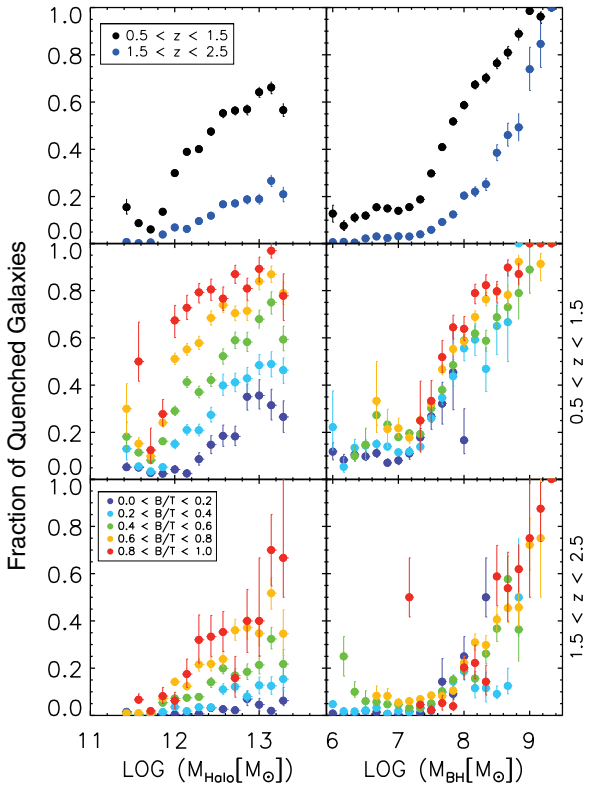

Figure 5. $f_{\rm quench}$ as a function of halo and black hole mass using galaxies from the Somerville et al. SAM. In the middle and bottom rows, the galaxy sample has been split in bins of B/T. Galaxies with sSFR $> 1/3 * t_{\rm Hubble}$ are assigned as star-forming, the others are assigned as quiescent. Uncertainties are derived via bootstrapping to reflect the sample variance.

(A color version of this figure is available in the online journal.)

however, the dependencies on the two look different. The increase in $f_{\rm quench}$ with $M_{\rm Halo}$ is gradual over nearly two orders of magnitude. In contrast, a much sharper upturn of $f_{\rm quench}$ emerges above $\log(M_{\rm BH}) = 7.5$. This behavior is especially notable at $z \sim 1$, but a rise above the same threshold is also present in the $z \sim 2$ population. Breaking the model galaxy population down by its structural properties, we find a wide spread in $f_{\rm quench}$ for different B/T at a given $M_{\rm Halo}$. A different, less scattered behavior would be expected if halo mass quenching were the sole and dominant mechanism (Birnboim et al. 2007; Dekel & Birnboim 2008; Dekel et al. 2009). However, as a function of $M_{\rm BH}$, a similar upturn in $f_{\rm quench}$ is present for all B/T bins equally above $\log(M_{\rm BH}) = 7.5$.

The increased scatter in the relation between $f_{\rm quench}$ and $M_{\rm bulge}$, compared to the tight correlation of $f_{\rm quench}$ and $M_{\rm BH}$ can be explained by the SAM's $M_{\rm BH}$–$M_{\rm bulge}$ relation. For a given B/T bin, the scatter in the $M_{\rm BH}$–$M_{\rm bulge}$ relation is significant compared to the dynamic range in the bulge masses plotted. At a given bulge mass, the scatter stems in part from an anti-correlation between the black hole mass and the level of star formation activity (sSFR).

Our analysis illustrates that in the Somerville model, which includes feedback from both supernovae and AGN, the central supermassive black hole acts as the primary agent of quenching in massive galaxies, and its accumulated mass (i.e., the integral over past accretion activity) is tightly related to the probability of finding a galaxy in a quenched state. Since the physical processes giving rise to bulge and black hole growth are the same in the SAM (mergers and disk instabilities), the stronger relation of

[22] See also Ciambur et al. (2013) for a discussion on the quenched fraction in the Garching SAMs.

$f_{\rm quench}$ with $M_{\rm bulge}$ than with M_*, present in both observations and model predictions, is not surprising.

We stress that in the Somerville model, no direct causal link between the presence of a bulge and quenching is implemented. The bulge is simply the accessible observable that correlates most tightly with the actual agent of quenching in this particular model: the supermassive black hole. Observationally, there is increasing evidence for AGN-driven outflows of massive $z \sim 1$–3 galaxies (Förster Schreiber et al. 2014; Nesvadba et al. 2011; Harrison et al. 2012; Cano-Díaz et al. 2012). Given the shortcomings of the SAM in a quantitative sense, notably its under-prediction of the quiescent population at $z \sim 2$, additional or other quenching processes may be at play in the real universe. One such process, which is causally linked to the presence of a bulge, could be morphological quenching (Martig et al. 2009; Genzel et al. 2014). In such a scenario, the high central stellar density provided by a bulge stabilizes the gas disk and prevents it from forming stars. While plausibly only a temporary measure (as no gas is expelled, or stopped from accreting through this mechanism), it could potentially contribute to suppressing star formation in $z \sim 2$ galaxies more efficiently and/or prevent them from returning to the star-forming branch in the SAM. In the local universe, star formation efficiencies of bulge-dominated systems are reduced by factors of ∼2–3 compared to disk-dominated galaxies (Saintonge et al. 2012; Martig et al. 2013).

6. DISCUSSION

6.1. Structural Change

In order to study the morphological differences between SFGs and QGs, and to draw conclusions on the possible structural changes of SFGs as they move along the MS, we first examined the mass dependence of the profile shape of SFGs and QGs as traced by the Sérsic index and B/T ratio. We have shown that QGs are structurally distinct from the star-forming population as seen by overall higher Sérsic indices and B/T ratios at a given stellar mass. SFGs show rising trends of their median Sérsic index and B/T ratio with increasing stellar mass, with the latter rising up to ∼40%–50% above $10^{11}\ M_\odot$. These findings give insights about the link between the structural evolution of SFGs and the quenching process as they move along the MS.

Analyzing the Schechter functional forms of the SFG and QG mass function as a function of redshift, Peng et al. (2010) conclude that the quenching rate of galaxies climbing the MS rises proportionally to the SFR (and given the near-linear MS slope therefore also proportionally to the stellar mass, hence their terminology "mass quenching"). This corresponds to a survival probability on the MS that drops exponentially with mass, implying that, while nearly all low-mass SFGs are destined to continue growing along the MS, toward the high-mass end the MS becomes progressively more dominated by nearly dead SFGs. In fact, the sub-unity slope of the MS, and possible flattening at the high-mass end (Whitaker et al. 2012), may well be interpreted in this context—the typical SFG above $10^{11}\ M_\odot$ is already undergoing some level of quenching, thereby deviating from the projected path along a SFR–mass relation of slope unity, which could be expected from cosmological accretion rates in the absence of quenching. Tying in our observational results on galaxy structure, the deviation toward high median n and B/T at the massive end reflects the typical structure of nearly dead star-formers that account for the bulk of SFGs above $10^{11}\ M_\odot$. The fact that they are structurally distinct implies that the morphological transition happens first, to be followed later by the departure from the MS. Bulge growth precedes quiescence. Such a morphological change prior to quenching is in line with qualitative predictions based on a toy model by Dekel & Burkert (2013). In the latter study, about half of the star-forming disk galaxies at $z \sim 2$ are predicted to evolve into compact star-forming "blue nuggets" due to violent disk instabilities before they are quenched into compact QGs ("red nuggets"). An observed population of "blue nuggets" has been proposed by Barro et al. (2013a, Barro et al. 2013b) to represent an evolutionary link, originating from extended disk galaxies and evolving into compact quiescent systems.

This does not refute that galaxies also undergo further structural evolution after they are quenched. At least part of the size growth (Cassata et al. 2013; van der Wel et al. 2014) and evolution toward rounder axial ratios (Chang et al. 2013) has been attributed to (minor and/or major) dry mergers, and it is conceivable that similar processes contribute to the observed trend of increasing B/T toward the massive end for the quiescent population.

6.2. AGN as the Driver of Quenching?

We have demonstrated that the bulge mass of a system is well correlated with its quenched state and has a stronger predictive power of quiescence than the total stellar mass. The observed trends of $f_{\rm quench}$ with total stellar mass, bulge mass, and disk mass as viewed among galaxies in different B/T bins are in good qualitative agreement with predictions from the Somerville et al. SAM. In the context of this model, the growth of the central supermassive black hole, which is the primary quenching agent for massive galaxies in this SAM, is tightly coupled with the growth of bulges through both merging and disk instabilities.

If a black hole—bulge scaling relation is in place during the peak of cosmic star formation as it is in the present-day universe (Häring & Rix 2004), our observational results together with the model comparison could therefore hint at the bulge not being the causal link to quenching, but rather the most accessible observational proxy for the AGN acting as the quenching agent.[23] In detail, however, there are quantitative differences between the SAM and our observations, most severely in the highest redshift bin ($1.5 < z < 2.5$), where the observed quenched fraction exceeds the value predicted by the SAM by a factor of ∼3.5. The latter difference could hint at a need for more frequent, efficient, or lasting quenching, a possible mechanism that we speculate about below. We also note that the same behavior is not necessarily a generic feature to all SAMs (see Appendix C).

It is tempting to draw connections between the emerging bulges in massive MS galaxies out to $z \sim 2.5$ revealed by our analysis, and recent observational results based on deep adaptive-optics-assisted integral field data sets and grism spectroscopy over the same redshift range. Förster Schreiber et al. (2014) found a high prevalence of powerful nuclear outflows in $\log(M) > 11$ galaxies driven by AGN, which appear to be absent in galaxies at lower masses. Along with star formation driven winds in the outer parts of the galaxies, such outflows could efficiently remove gas from the galaxies and, in this way, contribute to the quenching process.

[23] We note that Rosario et al. (2013) find X-ray signatures of AGN activity at these high redshifts to be most prominent among the star-forming population, most notably at the high-mass end, precisely where we see an upturn in the bulge fraction among SFGs.

Meanwhile, the 3D-HST and CANDELS legacy programs have yielded evidence for nuclear depressions in the Hα equivalent width in $z \sim 1$ SFGs (Nelson et al. 2012, 2013; Wuyts et al. 2013). At the highest stellar surface mass densities, star formation no longer appears to proceed in lockstep with the assembled stellar mass. Likewise, Genzel et al. (2014) report on ring-shaped Hα distributions in $z \sim 2$ SFGs, surrounding a more quiescent center where the dynamically inferred Toomre Q parameter significantly exceeds unity, owing to the emergence of a stellar bulge. Thus the Toomre stability criterion is satisfied in the central galaxy regions, which consequently could prevent the gas reservoir, if present there, from fragmenting and forming stars. While this result suggests that some causal connection between bulge growth and quenching may be at play, it should be noted (as is done also by Genzel et al. 2014) that gravitational quenching by itself does not expel the gas present, or stop the accumulation of a larger gas reservoir by continuing cosmological accretion. Additional maintenance modes might be required for a long-term shut down of further gas supply.

7. CONCLUSIONS

We analyzed the structural properties of a sample of 6764 massive ($>10^{10}$ $M_\odot$) galaxies in the redshift range $0.5 < z < 2.5$, by exploiting the multi-wavelength CANDELS *HST* imaging data set in all five CANDELS/3D-HST fields. We carried out single-component (Sérsic) fits and two-component (bulge + disk) decompositions, on stellar mass maps reconstructed from a resolved panchromatic SED modeling technique (Wuyts et al. 2012, 2013), as well as on images of the H-band surface brightness distribution. In addition, we compared our findings to predictions by the state-of-the-art SAM from Somerville et al. (2008, 2012; with extensions including disk instabilities presented by L. A. Porter et al. 2014, in preparation). Our main results are the following.

1. At fixed stellar mass, QGs have overall higher Sérsic indices and B/T ratios than SFGs as measured on their mass maps, in line with previous findings using monochromatic observations. We find an increase of Sérsic indices among SFGs with increasing total stellar mass, with the median mass profiles increasing from ($n \sim 1.3$) at 10^{10} $M_\odot$ to $n \gtrsim 2$ above 10^{11} $M_\odot$. Two-component bulge–disk decompositions confirm that the same rising trend is present when considering the median B/T ratio of SFGs, which is rising up to ~40%–50% above 10^{11} $M_\odot$. The same characteristic behavior is seen at $z \sim 1$ and $z \sim 2$.
2. Quantifying the same trends on the H-band light profiles, rather than the mass maps, the Sérsic indices and B/T fractions are overall lower for SFGs, confirming previous non-parametric measurements for a subset of our sample (Wuyts et al. 2012). The emergence of bulges above 10^{11} $M_\odot$ in SFGs appears to also be slightly less prominent when viewed in light, which is consistent with the steepest color gradients (blue disks with red central bulges) being found among massive SFGs.
3. The likelihood of a galaxy being quenched, as traced by the fraction of QGs, is better correlated with the bulge mass than the total stellar mass, and further shows no appreciable correlation with the amount of stellar mass in the disk component. The quenched fraction at redshift 1 is on average higher by a factor ~2 than at redshift 2.
4. At a given total stellar mass, the quenched fraction exhibits a strong positive correlation with B/T, while different B/T bins are confined to a significantly tighter locus in a diagram of $f_{\rm quench}$ versus $M_{\rm bulge}$. These findings imply that the bulge mass of a system is the single observable parameter with the most predictive power regarding its quenched state, although a somewhat tighter constraint on the probability of quiescence can be obtained if the total stellar mass is also known. The same trend is seen over the full redshift range probed, with the distinction that quenched fractions are lower at higher look-back times.
5. We find a good qualitative agreement between the SAM by Somerville et al. SAM and our observational findings. Since bulge and black hole growth are tightly coupled in the SAM, the strong dependence of $f_{\rm quench}$ on bulge mass follows rather naturally in this model. Our observational results can *in the context of this model* therefore be interpreted as the bulge being the closest observable proxy to the underlying agent of quenching: the black hole. Quantitatively, the largest discrepancy between the model and observations is found in the highest redshift bin ($1.5 < z < 2.5$), where the observed quenched fraction is larger by a factor of ~3.5 than predicted by the SAM. We note that the same behavior is not necessarily a generic feature to all SAMs.

The authors acknowledge fruitful discussions with Edmond Cheung, David C. Koo, Yu Lu, Casey J. Papovich, Mohammadtaher Safarzadeh, Benjamin J. Weiner, and Steven P. Willner. Support for Program number HST-GO-12060 and HST-GO-12177 was provided by NASA through a grant from the Space Telescope Science Institute, which is operated by the Association of Universities for Research in Astronomy, Incorporated, under NASA contract NAS5-26555.

APPENDIX A

THE MEANING OF A SÉRSIC INDEX MEASUREMENT

The combination of our one- and two-component fits on the mass maps enables us to empirically examine how the Sérsic index relates the amplitude of the bulge (as parameterized by B/T) on the one hand, and the relative size-ratio to the bulge and disk component ($R_{e,B}/R_{e,D}$) on the other hand. Figure 6 illustrates that, while B/T shows a clear correlation with n, there is no unique one-to-one translation between the two. Instead, the best-fit n to a composite bulge+disk system additionally depends on the size ratio of the two components. In other words, a galaxy's Sérsic index could be increased by placing more material in the bulge, but also by growing the disk at a fixed bulge size. The observed CANDELS galaxies occupy a surface in this three-parameter space (n, B/T, $R_{e,B}/R_{e,D}$) that is in good agreement with what would be anticipated from Sérsic fits to idealized, noise-free bulge ($n = 4$) plus disk ($n = 1$) profiles (squares and curves in the left- and right-hand panels of Figure 6, respectively). Evidently, for systems with B/T close to 0 or 1, the size ratio of the two components is ill-constrained, as one of them contains barely any mass. The galaxies in our full $0.5 < z < 2.5$ sample span the full range of B/T values, and are located predominantly around bulge-to-disk size ratios of $R_{e,B}/R_{e,D} \sim 0.2$.

APPENDIX B

COMPARISON WITH MEASUREMENTS ON H BAND

Here, we investigate how the results of our structural analysis change when conducting the measurements on the H-band light images, rather than on the stellar mass maps. To this end, we

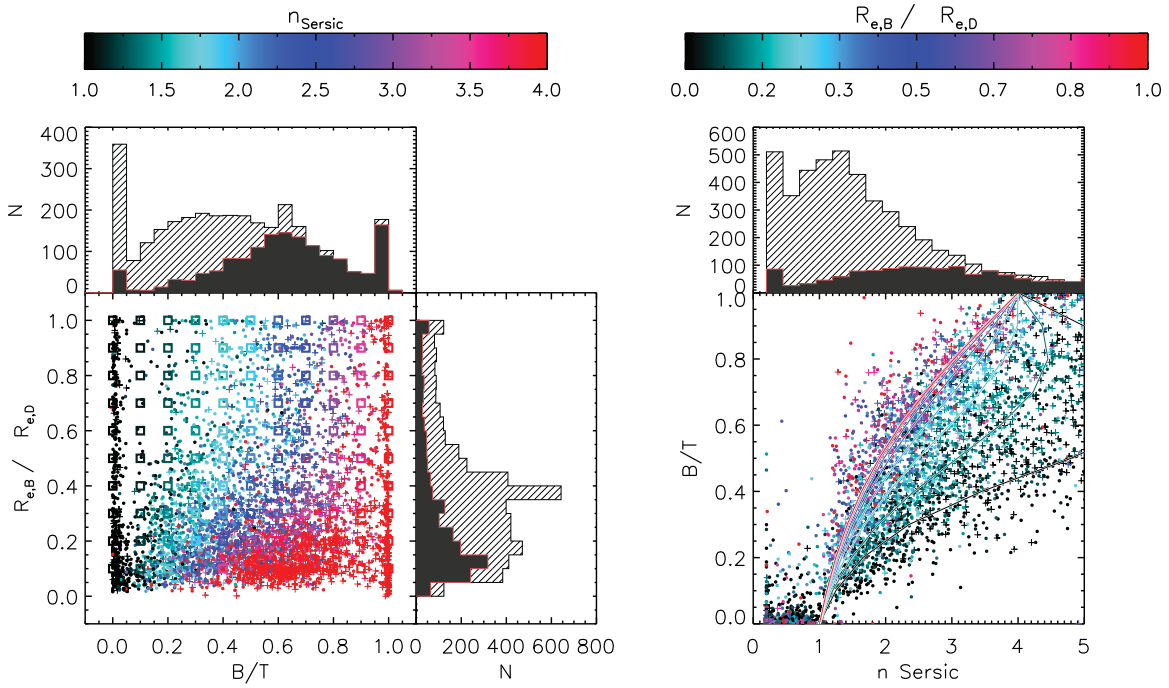

Figure 6. Left: size ratio between the bulge and disk component ($R_{e,B}/R_{e,D}$) vs. B/T for the whole galaxy sample as measured in mass. The color indicates the measured Sérsic index. Quiescent galaxies are shown as a plus (+), SFGs are shown as dots. Right: measured B/T values against Sérsic indices as seen in mass. The histograms show the respective measured distributions of B/T, $R_{e,B}/R_{e,D}$, and n among the sample for quiescent galaxies (solid black areas) and SFGs (hatched areas). The relationship between the Sérsic index and B/T is not unique, but rather crucially depends on $R_{e,B}/R_{e,D}$. The squares (left) and curved lines (right) illustrate the relation between (B/T, $R_{e,B}/R_{e,D}$) and n as inferred from noise-free idealized bulge + disk toy models, which are consistent with the trends seen for our observed galaxy samples.

(A color version of this figure is available in the online journal.)

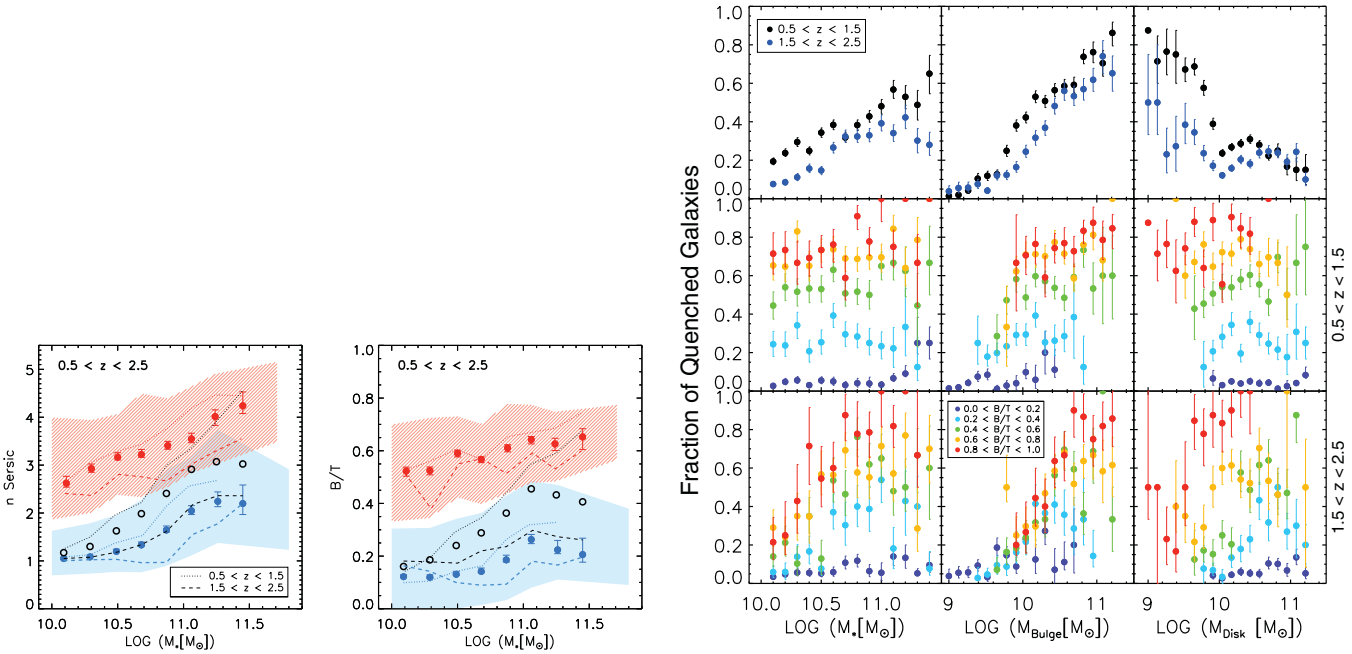

Figure 7. Equivalent of Figures 1 (left) and 3 (right) using the results of structural measurements on the *H*-band light images.

(A color version of this figure is available in the online journal.)

present in Figure 7 the same figures as discussed in Section 4, now using the Sérsic index and B/T values as inferred from the CANDELS *H*-band imaging. Likewise, we compute the bulge and disk mass as $(B/T)_H M_*$ and $(1-(B/T)_H)M_*$, respectively.

Overall, our analysis reveals a qualitatively similar mass dependence of n and B/T, and distinction between SFGs and QGs as inferred from the mass maps. In detail, however, modest changes in n and B/T are notable. While the median $z \sim 1$ (2) SFG has $(B/T)_H \lesssim 0.25$ (0.20), the typical bulge fractions increase to above 20%, and reach up to ~40%–50% at the massive end, once spatial M/L variations are corrected for. Likewise, the corresponding Sérsic indices measured on the

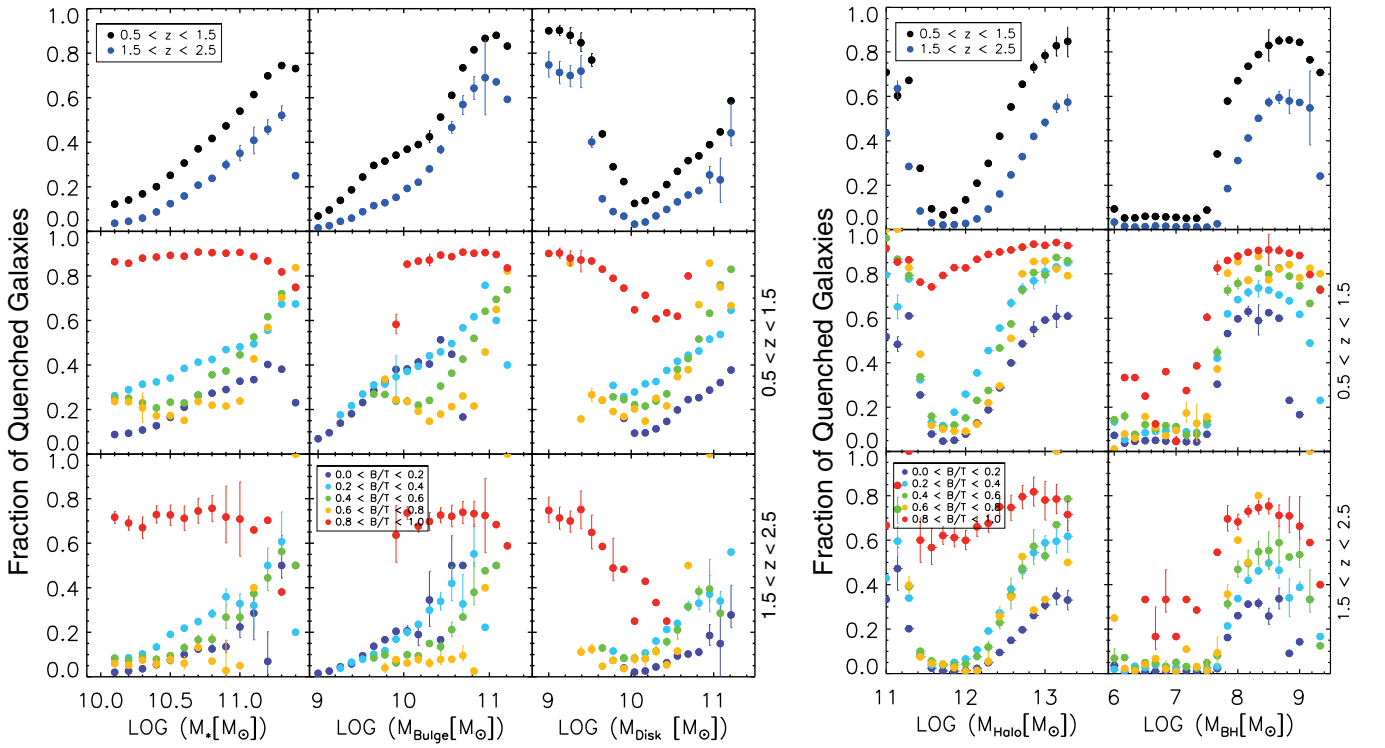

Figure 8. Fraction of massive galaxies ($M > 10^{10}\ M_{\odot}$) that are quiescent in the SAM of Guo et al. (2013), as a function of total stellar mass, stellar mass in the bulge and disk separately, and as a function of halo and black hole mass. The bottom two rows show the results split by bulge-to-total ratio, for the $z \sim 1$ and $z \sim 2$ bins, respectively.

(A color version of this figure is available in the online journal.)

H-band imaging for SFGs below $\log(M) = 10.8$ are consistent with the exponential disk profiles (see also Wuyts et al. 2011), but are slightly cuspier, as quantified on mass maps. This is in line with findings based on smaller subsets of CANDELS data by Wuyts et al. (2012) and Guo et al. (2012).

The central 50th percentile intervals marked by the red and blue polygons are somewhat less confined in the plots based on stellar mass maps compared to the H-band results. We interpret this to be due to an additional source of random uncertainty introduced by the resolved stellar population modeling. The resolved stellar population modeling itself was motivated by the need to reduce the systematic biases associated with spatial M/L ratio variations.

In Figure 7, the qualitative trends of $f_{\rm quench}$ with total stellar mass, bulge, and disk mass are very similar. However, the lower two rows of Figure 7 compared to Figure 3 show that the bins of the lowest and highest B/T are more separated from each other in $f_{\rm quench}$ in light than in mass. This observation is also in line with the disks of SFGs being dominating by a younger stellar population than that of the bulge, shifting SFGs to lower B/T. The middle panels of Figure 7 show a larger scatter than the corresponding panels in Figure 3.

APPENDIX C

COMPARISON TO GUO ET AL. SAM

In order to evaluate the extent to which the characteristic trends of the Somerville et al. SAM, as presented in Section 5, are generic to all SAMs, we considered an independent SAM by Guo et al. (2013). The Guo et al. (2013) model is rooted in the dark matter backbone of the Millennium Simulation (Springel et al. 2005), and its output tables with galaxy properties for snapshots of different look-back times are publicly available on the Virgo Millennium Database (Lemson & the Virgo Consortium 2006). We present the equivalent plots of Figures 4 and 5 in Figure 8. As in the Somerville model, quenched fractions are rising with increasing mass, increasing bulge mass, and decreasing redshift, but when broken down in bins of B/T, significant differences are notable. Specifically, $f_{\rm quench}$ does not monotonically increase with increasing B/T at a given stellar mass.

REFERENCES

Andredakis, Y. C., Peletier, R. F., & Balcells, M. 1995, MNRAS, 275, 874
Barro, G., Faber, S. M., Pérez-González, P. G., et al. 2013a, ApJ, 765, 104
Barro, G., Faber, S. M., Perez-Gonzalez, P. G., et al. 2013b, ApJ, submitted (arXiv:1311.5559)
Behroozi, P. S., Conroy, C., & Wechsler, R. H. 2010, ApJ, 717, 379
Bell, E. F. 2008, ApJ, 682, 355
Bell, E. F., van der Wel, A., Papovich, C., et al. 2012, ApJ, 753, 167
Bell, E. F., Wolf, C., Meisenheimer, K., et al. 2004, ApJ, 608, 752
Birnboim, Y., & Dekel, A. 2003, MNRAS, 345, 349
Birnboim, Y., Dekel, A., & Neistein, E. 2007, MNRAS, 380, 339
Bluck, A. F. L., Mendel, J. T., Ellison, S. L., et al. 2014, MNRAS, 441, 599
Bournaud, F., Dekel, A., Teyssier, R., et al. 2011, ApJL, 741, L33
Brammer, G. B., van Dokkum, P. G., Franx, M., et al. 2012, ApJS, 200, 13
Brammer, G. B., Whitaker, K. E., van Dokkum, P. G., et al. 2009, ApJL, 706, L173
Brammer, G. B., Whitaker, K. E., van Dokkum, P. G., et al. 2011, ApJ, 739, 24
Bruce, V. A., Dunlop, J. S., Cirasuolo, M., et al. 2012, MNRAS, 427, 1666
Bruce, V. A., Dunlop, J. S., McLure, R. J., et al. 2014, MNRAS, submitted (arXiv:1405.1736)
Bruzual, G., & Charlot, S. 2003, MNRAS, 344, 1000
Calzetti, D., Armus, L., Bohlin, R. C., et al. 2000, ApJ, 533, 682
Cano-Díaz, M., Maiolino, R., Marconi, A., et al. 2012, A&A, 537, L8
Cappellari, M., & Copin, Y. 2003, MNRAS, 342, 345
Cassata, P., Giavalisco, M., Williams, C. C., et al. 2013, ApJ, 775, 106
Chabrier, G. 2003, ApJL, 586, L133

Chang, Y.-Y., van der Wel, A., Rix, H.-W., et al. 2013, ApJ, 773, 149
Cheung, E., Faber, S. M., Koo, D. C., et al. 2012, ApJ, 760, 131
Ciambur, B. C., Kauffmann, G., & Wuyts, S. 2013, MNRAS, 432, 2488
Cibinel, A., Carollo, C. M., Lilly, S. J., et al. 2013, ApJ, 776, 72
Crocker, A., Krips, M., Bureau, M., et al. 2012, MNRAS, 421, 1298
Croton, D. J., Springel, V., White, S. D. M., et al. 2006, MNRAS, 365, 11
Daddi, E., Dickinson, M., Morrison, G., et al. 2007, ApJ, 670, 156
Davis, M., Guhathakurta, P., Konidaris, N. P., et al. 2007, ApJL, 660, L1
de Jong, R. S., Simard, L., Davies, R. L., et al. 2004, MNRAS, 355, 1155
Dekel, A., & Birnboim, Y. 2008, MNRAS, 383, 119
Dekel, A., Birnboim, Y., Engel, G., et al. 2009, Natur, 457, 451
Dekel, A., & Burkert, A. 2013, MNRAS, 438, 1870
Elbaz, D., Daddi, E., Le Borgne, D., et al. 2007, A&A, 468, 33
Elmegreen, B. G., Elmegreen, D. M., Fernandez, M. X., & Lemonias, J. J. 2009, ApJ, 692, 12
Faber, S. M., Willmer, C. N. A., Wolf, C., et al. 2007, ApJ, 665, 265
Fang, J. J., Faber, S. M., Koo, D. C., & Dekel, A. 2013, ApJ, 776, 63
Ferrarese, L., van den Bosch, F. C., Ford, H. C., Jaffe, W., & O'Connell, R. W. 1994, AJ, 108, 1598
Förster Schreiber, N. M., Genzel, R., Bouché, N., et al. 2009, ApJ, 706, 1364
Förster Schreiber, N. M., Genzel, R., Newman, S. F., et al. 2014, ApJ, 787, 37
Förster Schreiber, N. M., Shapley, A. E., Genzel, R., et al. 2011, ApJ, 739, 45
Franx, M., van Dokkum, P. G., Schreiber, N. M. F., et al. 2008, ApJ, 688, 770
Genzel, R., Förster Schreiber, N. M., Lang, P., et al. 2014, ApJ, 785, 75
Giavalisco, M., Ferguson, H. C., Koekemoer, A. M., et al. 2004, ApJL, 600, L93
Grogin, N. A., Kocevski, D. D., Faber, S. M., et al. 2011, ApJS, 197, 35
Guo, Y., Giavalisco, M., Cassata, P., et al. 2011, ApJ, 735, 18
Guo, Y., Giavalisco, M., Ferguson, H. C., Cassata, P., & Koekemoer, A. M. 2012, ApJ, 757, 120
Guo, Q., White, S., Angulo, R. E., et al. 2013, MNRAS, 428, 1351
Häring, N., & Rix, H.-W. 2004, ApJL, 604, L89
Harrison, C. M., Alexander, D. M., Swinbank, A. M., et al. 2012, MNRAS, 426, 1073
Hopkins, P. F., Hernquist, L., Cox, T. J., et al. 2006, ApJS, 163, 1
Hopkins, P. F., Somerville, R. S., Cox, T. J., et al. 2009, MNRAS, 397, 802
Ilbert, O., McCracken, H. J., Le Fèvre, O., et al. 2013, A&A, 556, A55
Jaffe, W., Ford, H. C., O'Connell, R. W., van den Bosch, F. C., & Ferrarese, L. 1994, AJ, 108, 1567
Kauffmann, G., Heckman, T. M., De Lucia, G., et al. 2006, MNRAS, 367, 1394
Kauffmann, G., Heckman, T. M., White, S. D. M., et al. 2003, MNRAS, 341, 54
Kennicutt, R. C., Jr. 1998, ApJ, 498, 541
Kereš, D., Katz, N., Weinberg, D. H., & Davé, R. 2005, MNRAS, 363, 2
Klypin, A. A., Trujillo-Gomez, S., & Primack, J. 2011, ApJ, 740, 102
Koekemoer, A. M., Aussel, H., Calzetti, D., et al. 2007, ApJS, 172, 196
Koekemoer, A. M., Faber, S. M., Ferguson, H. C., et al. 2011, ApJS, 197, 36
Koo, D. C., Simard, L., Willmer, C. N. A., et al. 2005, ApJS, 157, 175
Kormendy, J., & Kennicutt, R. C., Jr. 2004, ARA&A, 42, 603
Kriek, M., van Dokkum, P. G., Franx, M., Illingworth, G. D., & Magee, D. K. 2009, ApJL, 705, L71
Krist, J. 1995, in ASP Conf. Ser. 77, Astronomical Data Analysis Software and Systems IV, ed. R.A. Shaw, H.E. Payne, & J.J.E. Hayes (San Francisco, CA: ASP), 349
Lanyon-Foster, M. M., Conselice, C. J., & Merrifield, M. R. 2012, MNRAS, 424, 1852
Lee, B., Giavalisco, M., Williams, C. C., et al. 2013, ApJ, 774, 47
Lemson, G., & the Virgo Consortium, 2006, arXiv:astro-ph/0608019
Lu, Y., Wechsler, R. H., Somerville, R. S., et al. 2013, ApJ, submitted (arXiv:1312.3233)
Lutz, D., Poglitsch, A., Altieri, B., et al. 2011, A&A, 532, A90
Magnelli, B., Popesso, P., Berta, S., et al. 2013, A&A, 553, A132
Maraston, C., Pforr, J., Renzini, A., et al. 2010, MNRAS, 407, 830
Martig, M., Bournaud, F., Teyssier, R., & Dekel, A. 2009, ApJ, 707, 250
Martig, M., Crocker, A. F., Bournaud, F., et al. 2013, MNRAS, 432, 1914
Mo, H. J., Mao, S., & White, S. D. M. 1998, MNRAS, 295, 319
Moster, B. P., Somerville, R. S., Maulbetsch, C., et al. 2010, ApJ, 710, 903
Muzzin, A., Marchesini, D., Stefanon, M., et al. 2013, ApJ, 777, 18
Nelson, E. J., van Dokkum, P. G., Brammer, G., et al. 2012, ApJL, 747, L28
Nelson, E. J., van Dokkum, P. G., Momcheva, I., et al. 2013, ApJL, 763, L16
Nesvadba, N. P. H., Polletta, M., Lehnert, M. D., et al. 2011, MNRAS, 415, 2359
Noeske, K. G., Weiner, B. J., Faber, S. M., et al. 2007, ApJL, 660, L43
Papovich, C., Dickinson, M., & Ferguson, H. C. 2001, ApJ, 559, 620
Peng, C. Y., Ho, L. C., Impey, C. D., & Rix, H.-W. 2010, AJ, 139, 2097
Peng, Y.-j., Lilly, S. J., Kovač, K., et al. 2010, ApJ, 721, 193
Rodighiero, G., Daddi, E., Baronchelli, I., et al. 2011, ApJL, 739, L40
Rosario, D. J., Santini, P., Lutz, D., et al. 2013, ApJ, 771, 63
Saintonge, A., Tacconi, L. J., Fabello, S., et al. 2012, ApJ, 758, 73
Schiminovich, D., Wyder, T. K., Martin, D. C., et al. 2007, ApJS, 173, 315
Shapley, A. E., Steidel, C. C., Erb, D. K., et al. 2005, ApJ, 626, 698
Skelton, R. E., Whitaker, K. E., Momcheva, I. G., et al. 2014, ApJS, submitted (arXiv:1403.3689)
Somerville, R. S., Gilmore, R. C., Primack, J. R., & Domínguez, A. 2012, MNRAS, 423, 1992
Somerville, R. S., Hopkins, P. F., Cox, T. J., Robertson, B. E., & Hernquist, L. 2008, MNRAS, 391, 481
Springel, V., White, S. D. M., Jenkins, A., et al. 2005, Natur, 435, 629
Strateva, I., Ivezić, Ž., Knapp, G. R., et al. 2001, AJ, 122, 1861
Szomoru, D., Franx, M., van Dokkum, P. G., et al. 2010, ApJL, 714, L244
Szomoru, D., Franx, M., van Dokkum, P. G., et al. 2013, ApJ, 763, 73
Toft, S., Franx, M., van Dokkum, P., et al. 2009, ApJ, 705, 255
Tomczak, A. R., Quadri, R. F., Tran, K.-V. H., et al. 2014, ApJ, 783, 85
van den Bosch, F. C., Ferrarese, L., Jaffe, W., Ford, H. C., & O'Connell, R. W. 1994, AJ, 108, 1579
van der Wel, A., Bell, E. F., Häussler, B., et al. 2012, ApJS, 203, 24
van der Wel, A., Franx, M., van Dokkum, P. G., et al. 2014, ApJ, submitted (arXiv:1404.2844)
van Dokkum, P. G., Brammer, G., Fumagalli, M., et al. 2011, ApJL, 743, L15
Wang, T., Huang, J.-S., Faber, S. M., et al. 2012, ApJ, 752, 134
Weiner, B. J., Phillips, A. C., Faber, S. M., et al. 2005, ApJ, 620, 595
Whitaker, K. E., Labbé, I., van Dokkum, P. G., et al. 2011, ApJ, 735, 86
Whitaker, K. E., van Dokkum, P. G., Brammer, G., & Franx, M. 2012, ApJL, 754, L29
Williams, R. J., Quadri, R. F., Franx, M., van Dokkum, P., & Labbé, I. 2009, ApJ, 691, 1879
Windhorst, R. A., Cohen, S. H., Hathi, N. P., et al. 2011, ApJS, 193, 27
Woo, J., Dekel, A., Faber, S. M., et al. 2013, MNRAS, 428, 3306
Wuyts, S., Förster Schreiber, N. M., Genzel, R., et al. 2012, ApJ, 753, 114
Wuyts, S., Förster Schreiber, N. M., van der Wel, A., et al. 2011, ApJ, 742, 96
Wuyts, S., Förster Schreiber, N. M., Nelson, E. J., et al. 2013, ApJ, 779, 135
Wuyts, S., Labbé, I., Franx, M., et al. 2007, ApJ, 655, 51
Zibetti, S., Charlot, S., & Rix, H.-W. 2009, MNRAS, 400, 1181